Nanoscale

PAPER

View Article Online
View Journal

Cite this: DOI: 10.1039/d5nr04742k

Universal scaling formalism and analytical optimization criterion for multiscale geometric design of thermoelectric metamaterials

Xanthippi Zianni

Thermoelectric (TE) generators directly convert heat into electricity, yet their performance is often limited by small temperature gradients. Width-modulated metamaterials with constrictions and expansions (*constricted* geometries) sustain larger temperature differences ΔT than constant-width counterparts due to reduced *Transmissivity* (Tr) – the geometric ratio of constriction to expansion cross-sections. A scaling behavior of transport and key TE performance metrics with *Transmissivity* is demonstrated from the nanoscale to the macroscale using analytical formalism and simulations across single- and multiple-constriction profiles. It is shown that ΔT, electrical and thermal resistances, efficiency, and output power are governed by a single scaling function g(Tr) – the conductance of a constricted geometry relative to a uniform-width counterpart–independent of carrier type, material, or operating conditions. Universal scaling formalism leads to *Performance* Design *Maps* and an analytical optimization criterion: maximum TE performance occurs at an optimal *Transmissivity* Tr_{opt}, where $g(\mathrm{Tr}_{opt}) = \mathrm{Bi}$, with $\mathrm{Bi} = hL/k$ denoting the Biot number and h, L, and k the convection coefficient, length, and thermal conductivity, respectively. Compared with the uniform geometry, the optimal constricted geometry produces a maximum output power reduced under fixed ΔT, by a factor of Bi/4, and enhanced under identical convective operating conditions by a factor of $(1 + \mathrm{Bi})^2/(4\mathrm{Bi})$. This work provides a theoretical framework for multiscale design and optimization of *constricted* geometries, thereby enabling systematic exploration of design strategies for next-generation TE modules based on advanced thermoelectric metamaterials analogous to nature's hierarchical structures for optimized functionality.

Received 10th November 2025,
Accepted 21st March 2026

DOI: 10.1039/d5nr04742k

rsc.li/nanoscale

1. Introduction

Thermoelectric (TE) energy conversion directly transforms heat into electricity, offering a solid-state solution to energy and environmental challenges.[1–3] Thermoelectric devices, with their compact and scalable design, offer a sustainable response to the growing power demands of microelectronics, AI, autonomous sensors, and next-generation technologies by directly converting heat into electricity and recycling waste heat.[3–10]

The performance of TE devices is governed by a combination of properties of the material constituting the TE leg – primarily the figure of merit (ZT), which depends on the Seebeck coefficient, the electrical conductivity, and the thermal conductivity – as well as device-level factors such as maintenance of high temperature gradients with the use of efficient heat exchangers,[2,11,12] low contact/interface resistances to decrease output power losses[1,2,13–16] and alternatives to the traditional π-module geometry to meet the needs of various applications.[12,17–19] Although materials with high ZT values have been discovered, their integration into efficient modules remains limited due to unresolved technological challenges.[16] Today, a revolutionary shift in TE research recognizes material geometry as an independent factor capable of maximizing the thermal resistance of the leg and maintaining a high temperature difference, ΔT, under various operating conditions. Optimizing conventional TE leg geometry involves adjusting the height and cross-sectional area of a cuboid-shaped material to balance the requirements for high thermal resistance and low electrical resistance.[2,14,20] Non-cuboid shapes with variable cross-section – particularly *pyramidal* geometries – have drawn research interest in TEs since the early years of research,[21–23] but remained of limited focus until recent advances in metamaterials science and technology renewed attention. Width-modulated metamaterials featuring constrictions and expansions (*constricted* geometries) were proposed to increase the TE efficiency by geometrical tuning the electrical and thermal transport.[24–28] Research interest in *pyramidal*[29–32] and *constricted* geometries[33–35] has been reignited, theoretically demonstrating enhanced TE performance. Furthermore, significant progress in advanced manufacturing

Department of Aerospace Science and Technology, National and Kapodistrian University of Athens, Psachna, Evia, Greece. E-mail: xzianni@uoa.gr

techniques – such as additive manufacturing and Direct Ink Writing – enabled fabrication of non-conventional TE legs and initial experimental validation of predictions.[36,37] These findings sparked a surge of research on non-cuboid TE leg configurations.[38–53] Future advances will depend on multi-factor optimization of TE devices based on non-cuboid legs.[16,54,55] Optimizing metamaterial geometry with respect to TE performance metrics is a central prerequisite for advancing thermoelectric devices. Numerical studies have examined a wide range of non-cuboid shapes, demonstrating that variable cross-sections can improve performance under diverse boundary conditions and constraints (*e.g.*, constant volume, constant surface area).[33,35,37,43,46,56–58] Among these, *constricted* geometries consistently outperform cuboid and other variable cross-section designs.[34,35,37,49] Recent proposals for novel TE leg architectures – enabled by advanced manufacturing techniques – underscore the growing emphasis on enhancing TEG efficiency through geometry optimization, informed by high-fidelity simulations.[16] Despite this progress, three key challenges persist:[54] (i) an incomplete understanding of how shape governs the thermal and electrical resistances of metamaterials, (ii) the lack of validated optimization criteria applicable across different geometries, and (iii) the absence of standardized descriptors required for AI-driven design. The present work addresses these challenges introducing a physically grounded analysis, global optimization criteria, and performance metrics, supported by universal scaling formalism validated through finite element calculations across a range of geometry modulation profiles.

Geometry modulation affects transport on two distinct levels: material and structural. At the material level, it influences electric and thermal transport by modifying the energy states of electrons and phonons and altering their scattering.[24–26,59] At the structural level, transport is constrained by *reduced Transmissivity* – a mechanism arising purely from geometry, and fundamentally different from conventional boundary or interface scattering mechanisms.[27] The concept of *Transmissivity*, fully defined by the geometry-modulation profile, was first introduced as an intuitive framework for analyzing nanoscale thermal transport in *constricted* metamaterials.[27] Follow-up studies employing phonon Monte Carlo simulations validated these initial insights and uncovered distinct features associated with this mechanism.[28] A central finding was the characteristic scaling between thermal conduction and *Transmissivity*.[27,28] In this work, this concept is extended to the macroscale by demonstrating universal scaling dependence of electrical transport, thermal transport, and TE performance metrics on *Transmissivity* in constricted geometries with single- and multiple-constriction profiles at millimetric dimensions (Fig. 1). A universal scaling formalism is

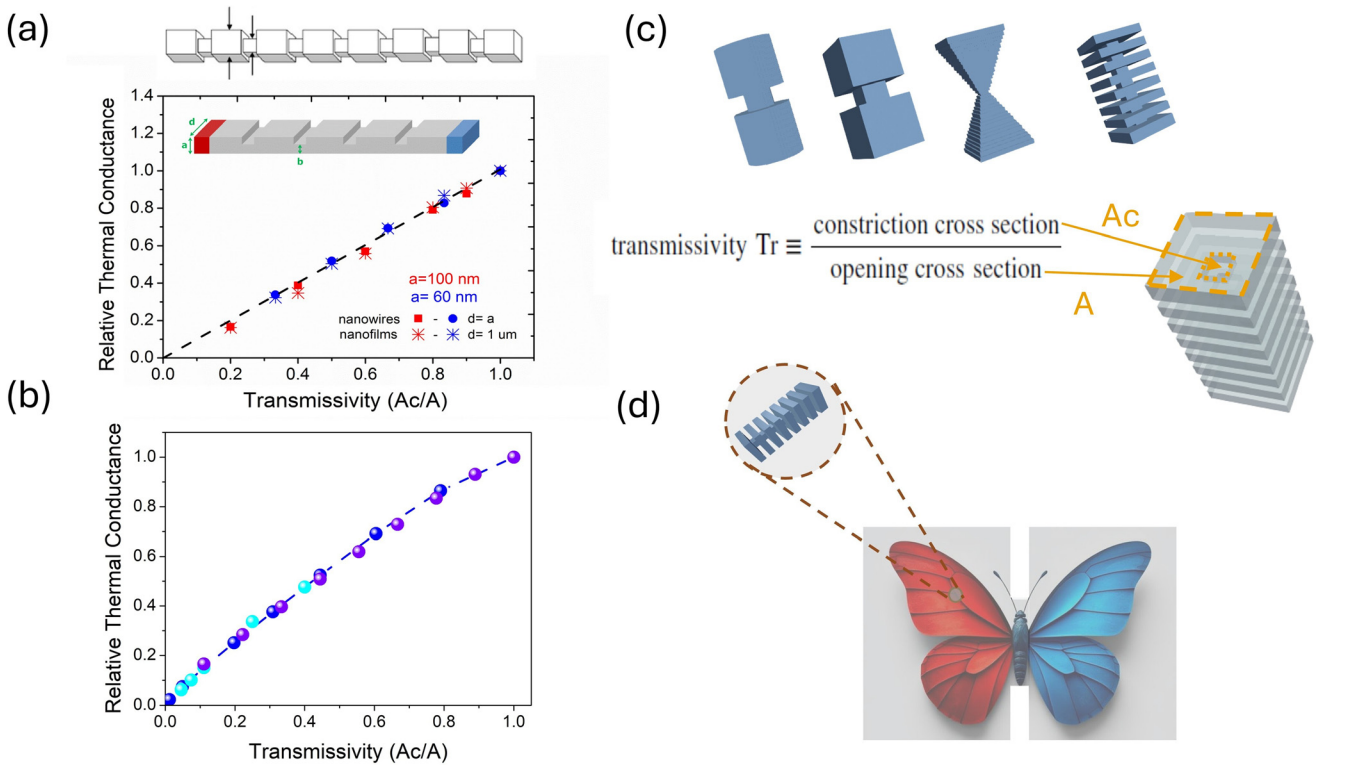

Fig. 1 Multiscale scaling with Transmissivity. Thermal conductance of width-modulated metamaterials *versus* Transmissivity (a) at the nanoscale,[28] and (b) at the macroscale, for dimensions detailed in Fig. 2. Thermal conductance is expressed relative to that of the constant-width material. (c) Definition of Transmissivity Tr as the ratio of the cross-sectional area of the constriction A_C to that of the expansion A. (d) Artistic representation of the concept of multiscale design of constricted metamaterials for energy convertors, reminiscent of nature-inspired designs that employ hierarchical scaling for optimized functionality.

developed, together with and an analytical performance optimization criterion in terms of *Transmissivity*, which is thereby established as a fundamental geometric descriptor enabling general multiscale design rules and global optimization criteria for enhancing TE performance.

Section 2 introduces the theoretical model and methodology. Section 3 presents and discusses the simulation results along with the analytical formalism, establishing universal scaling relations for electrical resistance, thermal resistance, temperature difference, efficiency and maximum output power with *Transmissivity*. It also introduces *Performance Design Maps*, formulates a global optimization criterion for maximizing the TE performance of metamaterials with *constricted* geometry and discusses the application of the geometry optimization formalism in connection with device-level factors and practical device design.

2. Method and validation

Calculations were carried out using the finite element method where the structure is discretized into individual cells. At two opposite sides of the material are imposed electrical potential difference ΔV and temperature difference ΔT. The current densities, **J**, and heat flux, **q**, are calculated using the following definitions:[2,14]

$$\mathbf{J} = -\sigma(\nabla V + S\nabla T) \quad (1)$$

$$\mathbf{q} = -k\nabla T + ST\mathbf{J} \quad (2)$$

where σ is the electrical conductivity, S is the Seebeck coefficient and k is the thermal conductivity of the material. The electrical potential, V, and the absolute temperature, T, profiles are determined applying electric current continuity and energy conservation conditions:

$$\nabla \cdot \mathbf{J} = 0 \quad (3)$$

$$\nabla \cdot \mathbf{q} = -\nabla V \cdot \mathbf{J}. \quad (4)$$

Calculations performed across different materials, dimensions, and temperature gradients consistently revealed the same trends. For clarity, we present representative results for n-type $Bi_2Te_{2.7}Se_{0.3}$ *constricted* geometries with single- and multiple-constriction modulation profiles. In the calculation, the experimentally measured[60] temperature dependence of the electrical conductivity, Seebeck coefficient, and thermal conductivity were used for the corresponding material parameters. The discretization of the structures varied depending on the complexity of the modulation and the length of the structure. For each geometry, the mesh was refined until further reduction of the cell size produced no change in the computed temperature and bias profiles. Convergence was assumed when additional refinement loops left these profiles unchanged and the continuity conditions were satisfied to within a few percent (typically 1–5%). A constant electrical bias was applied at the two opposite ends of the TE leg. Currents were then calculated as a function of the applied bias, and independent simulations were performed for a series of bias values to determine the current–voltage characteristics. The temperature at the hot side was fixed (eqn (38)). At the cold side, the boundary condition depended on the operating mode: the temperature was set equal to the ambient temperature T_a under fixed-temperature conditions, whereas eqn (39) was applied under convective cooling. Calculations were tested over a range of boundary-condition parameters. Representative results are presented for a hot-side temperature of T_h = 400 K, ambient temperature at T_a = 300 K and convection coefficients h = 200 Wm^{-2} K^{-1} (efficient convection) and h = 20 Wm^{-2} K^{-1} (weak convection).

Simulation results are interpreted by analytical formalism; their mutual comparison provides validation for both approaches. The finite-element simulations were also compared with recent experimental data, and very good agreement was obtained.[61] These experimental results were originally reported to be consistent with COMSOL simulations. Our calculations show quantitative agreement with those simulations as well as with other standard finite-element solvers widely used in the community, and can be readily reproduced using such tools. In addition, the Monte Carlo calculations were performed using an advanced simulator that is now publicly available.[62]

3. Results and discussion

3.1. Scaling of transport with Transmissivity

Evaluation of a TE device performance typically relies on the figure of merit ZT, the conversion efficiency, η, η_{max} and the maximum output power, P_{max}, of the material constituting the TE leg:[2]

$$ZT = \frac{\sigma S^2 T}{k} \quad (5)$$

$$\eta = \frac{P_{el}}{Q_{in}} \quad (6a)$$

$$\eta_{max} = \frac{\Delta T}{T_h}\frac{\sqrt{1+ZT}-1}{\sqrt{1+ZT}+\frac{T_c}{T_h}} \quad (6b)$$

$$P_{max} = \frac{{V_{OC}}^2}{4R_{el}} = \frac{S^2\Delta T^2}{4R_{el}} \quad (7)$$

where P_{el} is the electrical output power and Q_{in} is the incoming thermal power. V_{OC} is the open circuit voltage, $T_{h(c)}$ is the temperature of the hot (cold) side of the material, ΔT is the temperature difference across the structure and R_{el} is the material electrical resistance.

To improve TE efficiency, it is essential to enhance the intrinsic material's figure of merit ZT and maintain a large temperature difference ΔT across the material [eqn (6b)]. The value of ZT can be increased by engineering the material microscale morphology to optimize the transport properties: σ, S, and k. Preserving a high ΔT requires minimizing the

thermal conductance of the material G_{th} (or equivalently, maximizing the material's thermal resistance R_{th}), thereby reducing parasitic heat flow. This reduction can be achieved by lowering the material's intrinsic thermal conductivity at the microscale or by geometrically tuning G_{th} (R_{th}). Among various geometry design strategies, *constricted* geometry is a suitable approach because width-modulated materials by constrictions exhibit lower G_{th} than the corresponding G_{th}^{0} of constant-width cuboids. This was initially demonstrated in width-modulated nanostructures.[27,28] In particular, it was shown that the thermal conductance G_{th} of width-modulated nanoslabs (wires and films) decreases monotonically with decreasing the constriction width, relative to the conductance G_{th}^{0} of the corresponding uniform structure with constant width. For multiple-constriction modulation profiles (Fig. 1a), this monotonic reduction follows a simple analytical relation:[28]

$$\frac{G_{th}}{G_{th}^{0}} \sim \mathrm{Tr} \tag{8}$$

$$\mathrm{Tr} = \frac{A_C}{A} \tag{9}$$

where A and A_C are the cross-sectional areas of the expansions and the constrictions respectively (Fig. 1). Tr defined as the ratio of the two characteristic cross-sections of the modulated material, expresses the *Transmissivity* of the actual constricted geometry.[27,28] This definition should be appropriately modified for other metamaterial geometries.

Eqn (8) makes it explicit that in *constricted* geometries G_{th} is smaller than G_{th}^{0} because the constriction area A_C is smaller than the expansion area A(Tr < 1). Moreover, this equation shows that the ratio G_{th}/G_{th}^{0} scales directly with Tr, *i.e.* the decrease in G_{th} relative to G_{th}^{0} is governed by the ratio A_C/A. Consequently, the relative decrease in thermal conductance induced by geometric modulation will be identical across structures with different absolute values of A (or A_C) as long as they have the same Tr.

The scaling of thermal conductance with *Transmissivity* holds irrespective of the modulation profile, although the exact functional dependence is dictated by the specific form of that profile.[28,63,64] Eqn (8) can therefore be recast in a more general form to account for this dependence:

$$\frac{G_{th}}{G_{th}^{0}} = g(\mathrm{Tr}) \tag{10}$$

where g(Tr) denotes the functional dependence of G_{th}/G_{th}^{0} on Tr.

The reduction of G_{th} in *constricted* metamaterials, relative to G_{th}^{0}, can be fully attributed to the decreased *Transmsissivity* imposed by the modulation geometry. The scaling dependence of the relative conductance G_{th}/G_{th}^{0} on Tr – a quantity deter-

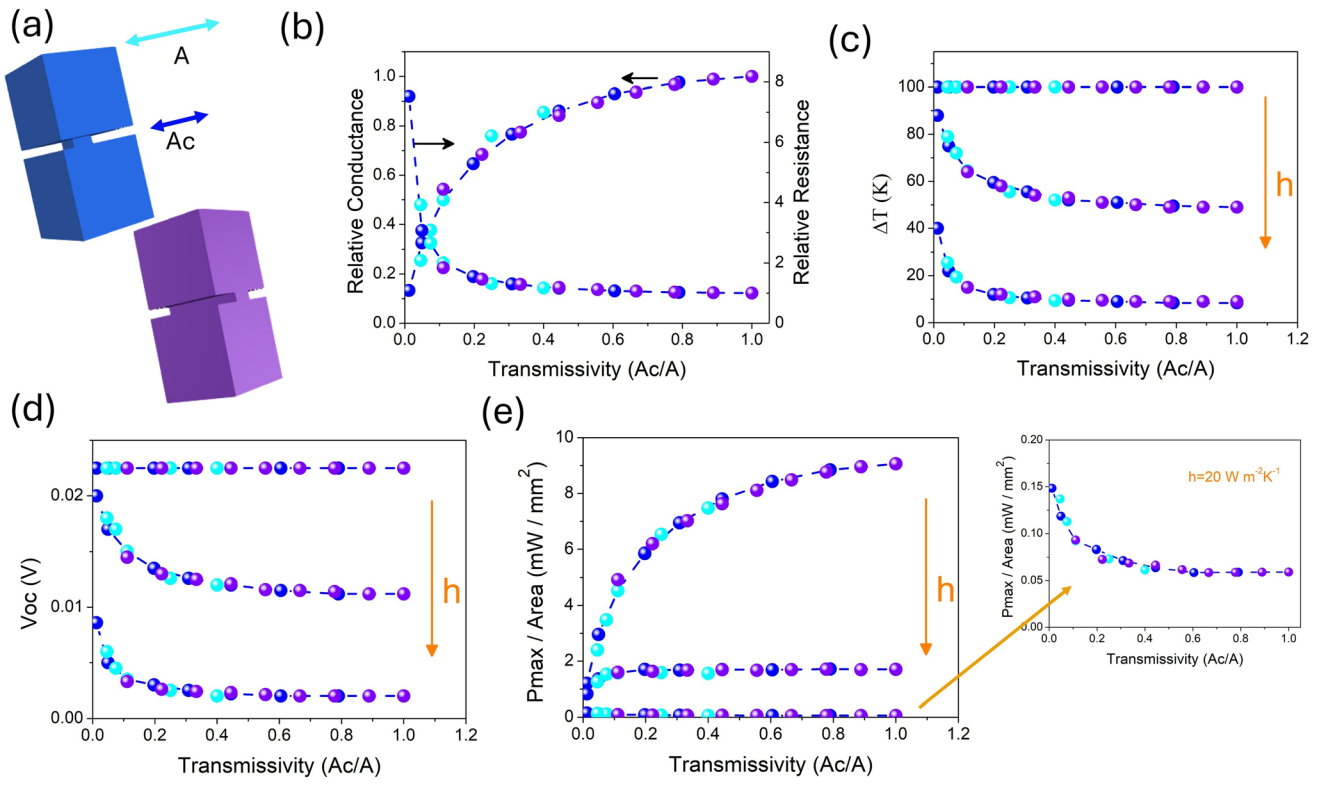

Fig. 2 Scaling behavior for single-constriction width-modulation. (a) Calculations for structures with 1D (purple) and 2D (blue and cyan) width-modulation geometries. (b) Relative (electrical and thermal) conductance/resistance. (c) Temperature difference ΔT. (d) Open-circuit voltage V_{OC}. (e) Maximum output power density P_{max}/A, under three operating conditions with decreasing convection coefficient: $h = \infty$ (fixed ΔT), 200 Wm^{-2} K^{-1}, and 20 Wm^{-2} K^{-1}. The inset in (e) corresponds to h = 20 Wm^{-2} K^{-1}. Two modulation schemes are compared: fixed A = 4 mm × 4 mm with variable A_C (blue and purple symbols), and fixed A_C = 2 mm × 2 mm with variable A (cyan symbols). The structure length L is fixed at 8 mm.

mined solely by geometry – reflects the geometric origin of the reduced thermal conductance in this class of metamaterials. This scaling behavior has been consistently observed across different nanoscale modulation profiles.[28,63,64]

Here, this behavior is demonstrated in *constricted* materials with millimetre-scale dimensions, as in typical TE legs. Finite element calculations were performed varying cross-sectional areas A and A_C. Representative results are shown for single-constriction (Fig. 2) and multiple-constriction modulation profiles (Fig. 3), under both one- (1D) and two- (2D) dimensional width-modulation schemes (Table 1): (i) varying A while keeping A_C fixed, and (ii) varying A_C with A held constant. In all cases, the simulations confirm that $G_{th}/G_{th}{}^0$ scales with Tr.

Notably, electrical conductance exhibits the same dependence on Tr as thermal conductance. Regardless of the absolute values of thermal or electrical resistance, the normalized ratios $G_{th(el)}/G_{th(el)}{}^0$ follow the same functional form g(Tr) (Fig. 4). This universality observed across all modulation profiles (Fig. 2–4) indicates that the impact of geometry modulation on transport is inherently geometric and independent of the nature of carriers. Hence, it holds:

$$\frac{G_{el}}{G_{el}{}^0} = g(\mathrm{Tr}). \tag{11}$$

Eqn (10) and (11) make explicit that, in *constricted* metamaterials electrical and thermal conduction remain coupled similarly as in uniform materials, meaning that geometry modulation by itself does not offer a way around the persistent trade-off between them.

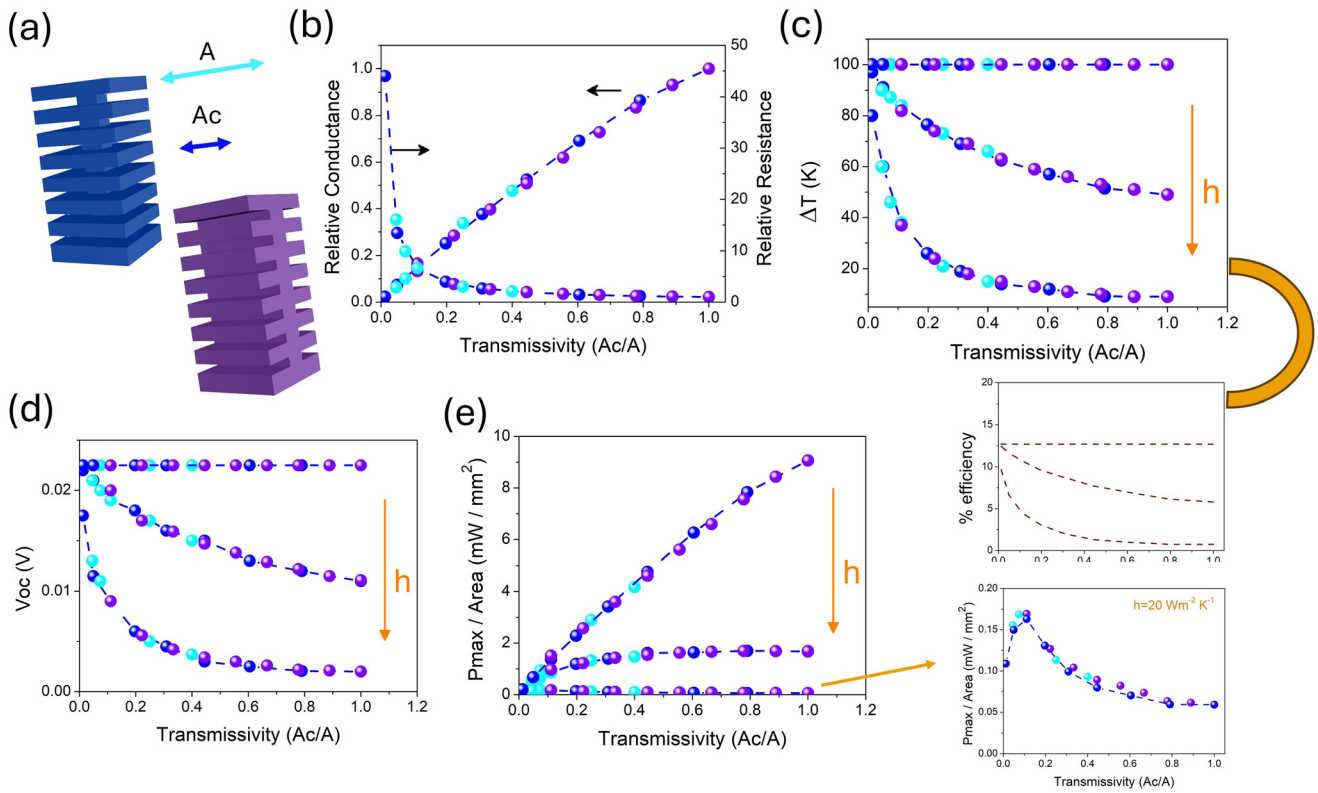

Fig. 3 Scaling behavior for multiple-constriction width-modulation. (a) Calculations for structures with 1D (purple) and 2D (blue and cyan) width-modulation geometries. (b) Relative electrical and thermal conductance/resistance. (c) Temperature difference ΔT and efficiency n_{max}. (d) Open-circuit voltage V_{OC}. (e) Maximum output power density P_{max}/A, under three operating conditions with decreasing convection coefficient: $h = \infty$ (fixed ΔT), 200 Wm^{-2} K^{-1}, and 20 Wm^{-2} K^{-1}. The inset in (e) corresponds to h = 20 Wm^{-2} K^{-1}. Symbol colours and structures dimensions are identical to those presented in Fig. 2.

Table 1 Classification of geometry types and modulation schemes

Geometry class	Modulation scheme	Figure	Color coding
Single constriction	1D and 2D	Fig. 2	1D: purple; 2D: blue and cyan
Multiple constrictions	1D and 2D	Fig. 3	1D: purple; 2D: blue and cyan
Modulation strategy A	Vary A_C with A fixed	All figures	Blue and purple symbols
Modulation strategy B	Vary A with A_C fixed	All figures	Cyan symbols

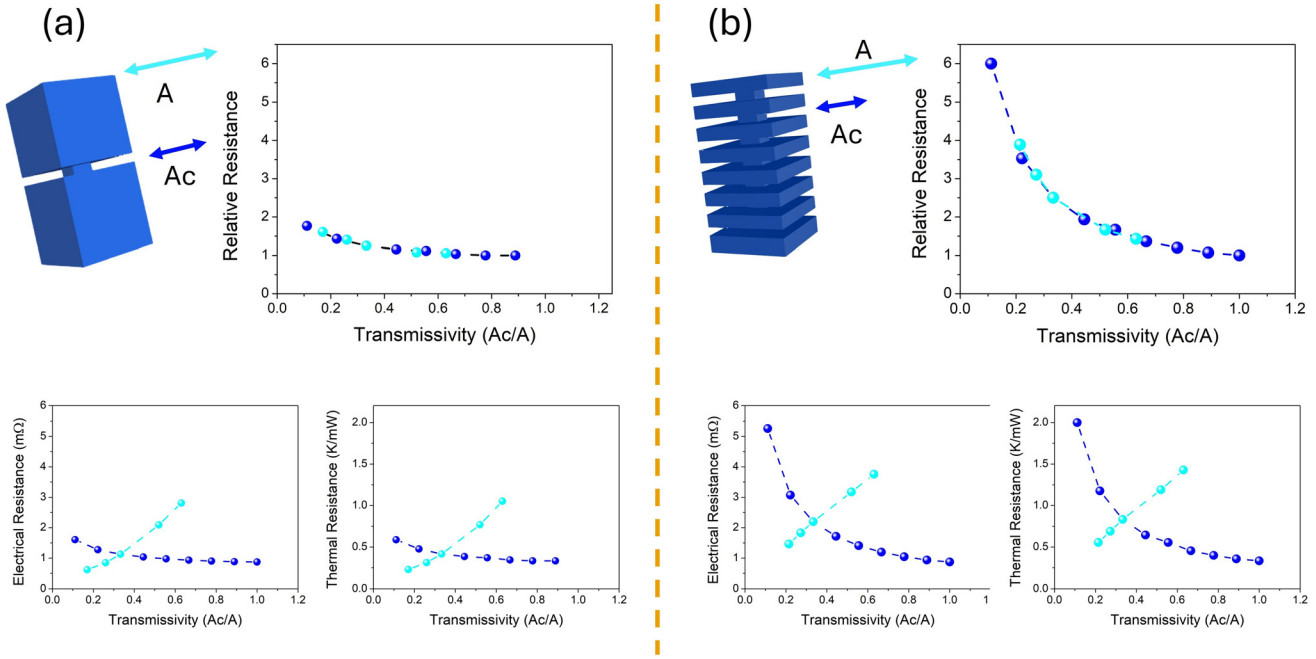

Fig. 4 Scaling of resistance with Transmissivity. Electrical and thermal resistances – shown both in absolute terms and normalized to the constant cross-section structure $R_{th(el)}/R_{th(el)}{}^{0}$ – as a function of Transmissivity for width-modulated structures with: (a) single-constriction and (b) multiple-constriction profiles. Blue and cyan symbols correspond to the two modulation schemes described in the caption of Fig. 2.

The functional form $g(\mathrm{Tr})$ is determined by the specific modulation profile. Both nanoscale[28,63,64] and macroscale calculations, indicate the following approximate relation:

$$g(\mathrm{Tr}) \sim \mathrm{Tr}^{n} \tag{12}$$

with $n \approx 1$ for multiple-constriction modulation and $n \approx 0.5$ for single-constriction modulation.

These scaling exponents are consistent with the underlying physics. For a single constriction, the dominance of constriction (spreading) resistance in the 3D solution of Laplace's equation leads to an effective conductance scaling as $G \propto \sqrt{A_C}$, implying $g(\mathrm{Tr}) \propto \mathrm{Tr}^{0.5}$. For a series of constrictions along the current path, the current is repeatedly 'pinched' and never fully spreads into the volume of the intervening expansions. The effect depends on the modulation degree (constriction density).[28,64] When the constriction modulation is sufficiently dense, the structure behaves effectively as a resistor of cross section A_C giving $G \propto A_C$ and therefore $g(\mathrm{Tr}) \propto \mathrm{Tr}$.

This behaviour holds at both the macroscale and the nanoscale within the diffusive transport regime that dominates in good TE materials. At the macroscale, this has been demonstrated through finite-element analysis, which is well suited for macroscopic transport and which we used to understand and optimize width-modulated TE legs with millimetric features. At the nanoscale, additional mechanisms – such as boundary scattering, size-dependent thermal conductivity, and non-diffusive (ballistic or quasi-ballistic) transport – become important. These effects have been examined in our previous work using Monte Carlo simulations, which are appropriate for nanoscale transport and for analysing width-modulated nanostructures. These studies showed that the conductance-scaling behaviour holds at the nanoscale and that size-dependent effects are captured by the uniform-width nanomaterial conductivity.[28] Deviations from this scaling behavior are expected in the single-constriction regime in nanostructures whose dimensions fall well below the carriers mean free paths. Electron mean free paths in typical TE materials are on the order of 1 nm. For example, in crystalline Bi_2Te_3 the electron mean free path – depending on doping – lies in the range of 2–5 nm at 500 K. In nanostructured TE materials, this mean free path may be further reduced due to distorted crystallinity, allowing electron transport to be safely treated as diffusive. Large phonon mean free paths contribute significantly to thermal transport in materials with high thermal conductivity. In good TE materials, which have low thermal conductivity, phonons with short mean free paths dominate heat transport. For instance, crystalline Bi_2Te_3 has a thermal conductivity of order 1 Wm^{-1} K^{-1}, corresponding to phonon mean free path of roughly 1 nm. In nanostructures, contributions from phonons with long paths are suppressed by scattering at defects, boundaries, and interfaces – one of the key reasons nanostructuring is an effective strategy for reducing thermal conductivity and enhancing TE performance. Consequently, ballistic phonon effects are not expected to dominate in nanostructured TE materials, and thermal transport can be treated as diffusive when optimizing constricted TE legs with nanoscale features.

The relative conductance $G_{th(el)}/G_{th(el)}{}^{0}$ decreases monotonically with decreasing Tr (Fig. 2b and 3b). In contrast, the absol-

ute values of conductance (or resistance) may not vary monotonically with Tr, as the outcome depends on which dimension is held constant. This effect is illustrated in Fig. 4 where resistance is shown in both absolute and relative terms. Specifically, resistance increases with decreasing Tr when A_C decreases at fixed A, whereas it decreases with decreasing Tr when A increases at fixed A_C. These opposite trends arise because, in the first case, $R_{th(el)}{}^0$ remains constant, and resistance is governed solely by the variation in Tr due to varying A_C. In the second case, however, $R_{th(el)}{}^0$ itself varies with A, so resistance is primarily determined by the increase in $R_{th(el)}{}^0$ as A decreases.

The demonstrated scaling dependence has been validated across different materials and temperature gradients, confirming that *varying Transmissivity* serves as a purely geometric mechanism for tuning conduction. This mechanism is thus distinct from conventional mechanisms such as intrinsic scattering or boundary/interface roughness scattering, which depend on carrier type and intrinsic material properties. The consistent scaling behavior of transport with Tr – across length scales from the nanoscale to the macroscale–demonstrates that *Transmissivity* reflects a geometric property of the constricted metamaterial rather than a simple geometric ratio. For example, assigning the same numerical ratio A_C/A to *pyramidal* geometries would not capture the physical essence of *Transmissivity*. Owing to this scaling relationship, the reduction (increase) in conductance (resistance) in a constricted metamaterial relative to the corresponding uniform material can be fully determined by this geometric property, positioning *Transmissivity* as a robust descriptor of the effect of geometry modulation on transport across multiple scales.

These results establish that conduction in *constricted* metamaterials exhibits a universal scaling dependence on *Transmissivity* – independent of transport carrier (electrons or phonons), intrinsic material properties, or specific modulation profile.

3.2. Scaling of ΔT and TE efficiency with Transmissivity

The efficiency of a TE module is governed by the temperature difference ΔT across the leg material [eqn (6b)]. This difference reaches its maximum under fixed contact temperature conditions. In practical operating environments, however, contact temperatures often fluctuate due to convective heat exchange. Under such convective conditions, the contact temperature is determined by both the thermal resistance R_{th} of the leg and the strength of convective flow – quantified by the convection heat transfer coefficient, h. For uniform materials, it can be shown (Appendix A) that:

$$\Delta T = \frac{hL}{k + hL}\Delta T_{max} \quad (13)$$

where $\Delta T_{max} \equiv T_h - T_a$. L denotes the length of the material along the temperature gradient.

A higher value of h corresponds to stronger heat exchange, causing the contact temperature to approach that of the ambient. In the theoretical limit $h \to \infty$, the contact temperature equals that of the environment yielding $\Delta T = \Delta T_{max}$. As h decreases, the attainable ΔT is reduced, a well-known challenge for TE devices operating under weak convection. This relationship is captured by eqn (13) and is confirmed by the finite element calculations for constant-width geometries ($A_C = A$ and Tr = 1) (Fig. 2c and 3c). The thermal conductivity is weakly temperature dependent.[60] Simulations show exact quantitative agreement with eqn (13) when using the average thermal conductivity k = 1.8 Wm^{-1} K^{-1} and the length L = 8 mm of the simulated structures.

Finite element calculations indicate that, under convective conditions ΔT is higher in constricted materials ($A_C < A$ and Tr < 1) than in the corresponding uniform material with constant cross-section A (Fig. 2c and 3c). This demonstrates that the temperature difference ΔT diminishes less (is preserved better) in *constricted* geometries compared to their cuboid counterparts under the same convective operating conditions. Importantly, ΔT increases monotonically as Tr decreases, reflecting the concurrent increase of the relative thermal resistance ($R_{th}/R_{th}{}^0$) and exhibits a direct scaling relationship with Tr. These simulation results are further validated by the following analytical formalism obtained by extending eqn (13) to non-uniform materials (Appendix A):

$$\Delta T = \frac{hL/k}{G_{th}/G_{th}{}^0 + hL/k}\Delta T_{max}. \quad (14)$$

Eqn (14) and finite element calculations show quantitative agreement across all simulated structures (Tr ≤ 1). The simulation results in Fig. 2c and 3c match exactly the predictions of eqn (14) when using k = 1.8 Wm^{-1} K^{-1}, L = 8 mm and the calculated values of $G_{th}/G_{th}{}^0$ in Fig. 2b and 3b.

Eqn (14) makes clear that the enhancement of ΔT arises from the reduced relative thermal conductance $G_{th}/G_{th}{}^0$, which is directly governed by the smaller *Transmissivity* of the constricted geometry. It also interprets the scaling of ΔT with Tr observed in the simulations, showing that it originates from the scaling dependence of $G_{th}/G_{th}{}^0$ on Tr. A key implication of this scaling is that structures with identical modulation ratios (A_C/A) – and thus the same Tr – will exhibit the same ΔT, regardless of their absolute cross-sectional areas. This leads to the important conclusion that, for fixed h, L and k, ΔT is determined by the *Transmissivity* of the material *constricted* geometry.

A comparison of the results for a given h (Fig. 2c and 3c) shows that ΔT rises more sharply with decreasing Tr in multiple-constriction modulations than in single-constriction cases. This behavior stems from the fact that $G_{th}/G_{th}{}^0$ is lower in structures with multiple constrictions than in those with a single constriction at the same Tr (Fig. 2b and 3b). As the number of constrictions increases, conductance decreases (and resistance increases) progressively with the degree of modulation.[62] Consequently, geometries with more extended modulation yield a more pronounced increase in ΔT as Tr decreases.

At the macroscale, the figure of merit ZT remains constant since the intrinsic material transport properties (σ, k and S) are independent of the material dimensions. As a result, the

TE efficiency directly follows the behavior of ΔT [eqn (6b)]. The maximum efficiency η_{max} increases monotonically as Tr increases (Fig. 3c). Like ΔT, η_{max} also scales with Tr, owing to its dependence on the ratio G_{th}/G_{th}^{0}, as captured by the following analytical expression derived from eqn (6b) and (14):

$$\eta_{max} = \frac{\Delta T_{max}}{T_h}\frac{\sqrt{1+ZT}-1}{\sqrt{1+ZT}+1-\frac{\Delta T_{max}}{T_h}\frac{hL/k}{G_{th}/G_{th}^{0}+hL/k}}\frac{hL/k}{G_{th}/G_{th}^{0}+hL/k} \quad (15)$$

From eqn (10), (14) and (15), universal scaling relations for ΔT and η_{max} can be derived in terms of the same function g(Tr):

$$\Delta T = \frac{hL/k}{g(\mathrm{Tr})+hL/k}\Delta T_{\max} \quad (16)$$

$$\eta_{\max} = \frac{\Delta T_{\max}}{T_h}\frac{\sqrt{1+ZT}-1}{\sqrt{1+ZT}+1-\frac{\Delta T_{\max}}{T_h}\frac{hL/k}{g(\mathrm{Tr})+hL/k}}\frac{hL/k}{g(\mathrm{Tr})+hL/k} \quad (17)$$

The optimization of the *constricted* geometry is strongly dictated by its *Transmissivity*, which serves as a key design parameter. Enhancement in TE efficiency [eqn (6b)] arises primarily from the elevated thermal resistance R_{th}, compared with R_{th}^{0}. Eqn (14) explicitly shows that the increase (decrease) in R_{th} (G_{th}) directly enhances the temperature difference ΔT under convective operation. To explore the role of the constriction, the data of Fig. 2c for ΔT due to a single-constriction modulation are re-plotted against the inverse Transmissivity (Tr^{-1}) (Fig. 5b). Then, a distinct progression is observed regardless of the specific constriction profile – whether abrupt or gradual (Fig. 5a): an abrupt growth in ΔT is followed by saturation, where the plateau asymptotically approaches the ambient temperature. This saturation limit is prescribed by eqn (14), which identifies the convection coefficient h, material conductivity k, and length L as the key determinants of the plateau height. The emergence and extent of the plateau are governed by the functional g(Tr) [eqn (16)], thereby linking the phenomenon directly to geometric *Transmissivity*.

Analysis of the temperature distribution (T-profile) across the constricted material provides further insight into the underlying mechanism for the occurrence of the plateau (Fig. 5b). For large Tr, the T-profile is nearly linear. As Tr decreases, however, it progressively distorts and eventually develops into a broad, stable window centered at the constriction. By Fourier's law, thermal conductivity is inversely related to the local temperature gradient. Thus, the sharp gradient appearing at the constriction at the onset of the plateau signals the formation of a dominant thermal resistance. This localized resistance, referred to as Constriction Thermal Resistance (CTR), first identified at the nanoscale (Fig. 5d)[28] and demonstrated here at the macroscale (Fig. 5c) – remains nearly constant within the plateau regime, as indicated by the weak variation in T-profiles across different Tr values. The formation of CTR accounts for the abrupt rise in ΔT below a critical Tr. As a result, maximum TE efficiency is achieved at the onset of this plateau, marking the transition into the CTR-dominated regime.

3.3. Scaling of the output power density with Transmissivity

The maximum output power P_{max} is governed by the trade-off between the open-circuit voltage V_{OC} and the electrical resistance R_{el} [eqn (7)]. V_{OC} is directly proportional to ΔT following the relation: $V_{OC} = S\Delta T$. The calculated values of V_{OC} (Fig. 2d and 3d) are fully consistent with this relation. Moreover, the spatial distribution of voltage across the constricted material mirrors the corresponding temperature distribution (Fig. 6).

Under fixed ΔT, P_{max} of a constricted material is lower than that of the corresponding uniform material P_{max}^{0}. This occurs because V_{OC} remains unchanged, while R_{el} is reduced relative

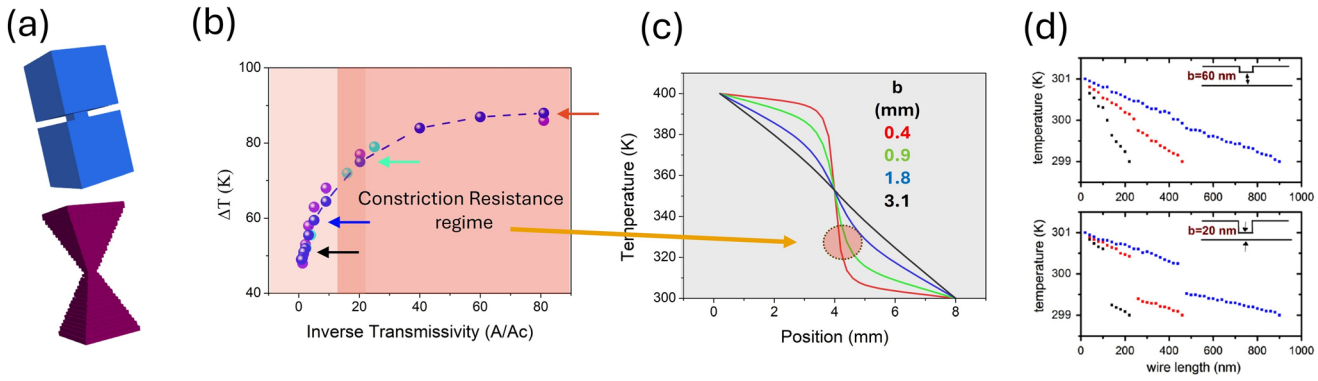

Fig. 5 Constriction Thermal Resistance across scales. (a) Abrupt (blue) and smooth (violet) constriction geometries. (b) Temperature difference ΔT *vs.* inverse Transmissivity (Tr^{-1}) for single-constriction structures: fixed A with variable A_C (blue, purple and violet), and fixed A_C and variable A (cyan), for dimensions as in Fig. 2. (c) Formation of Constriction Thermal Resistance (CTR) at the macroscale. (d) Formation of CTR at the nanoscale (adapted from ref. 28).

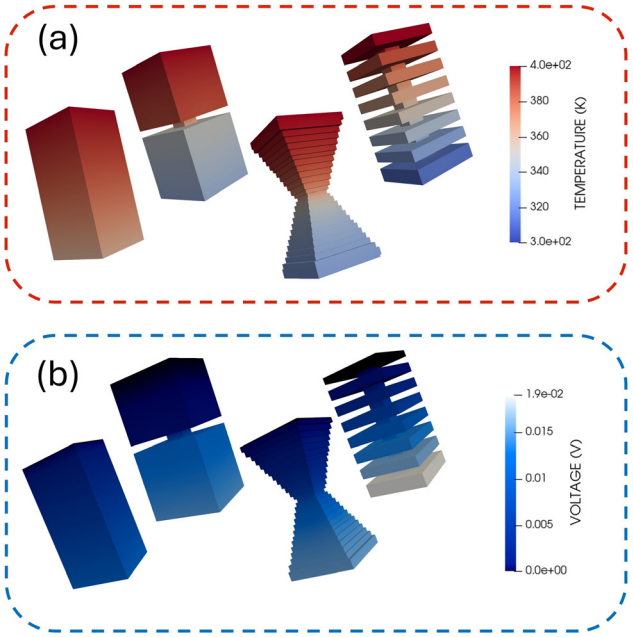

Fig. 6 Temperature and voltage distribution. (a) Temperature and (b) Voltage profiles across different *constricted* geometries under the same convective operating conditions.

to $R_{el}{}^0$. This relationship is made explicit by the following expression derived from eqn (7):

$$P_{max} = \frac{P_{max}{}^0}{R_{el}/R_{el}{}^0} = P_{max}{}^0(G_{el}/G_{el}{}^0) = P_{max}{}^0 g(\mathrm{Tr}) \quad (18)$$

$$P_{max}{}^0 = \frac{S^2 \Delta T_{max}{}^2}{4R_{el}{}^0}. \quad (19)$$

Eqn (18) shows that the ratio $P_{max}/P_{max}{}^0$ is directly proportional to $G_{el}/G_{el}{}^0$, and therefore decreases as Tr is reduced. Furthermore, $P_{max}/P_{max}{}^0$ follows the same scaling dependence on Tr, governed by the function g(Tr).

From eqn (19) it is obtained:

$$P_{max}{}^0 = A\frac{\sigma S^2 \Delta T_{max}{}^2}{4L}. \quad (20)$$

Eqn (18) and (20), give:

$$\frac{P_{max}}{A} = \frac{\sigma S^2 \Delta T_{max}{}^2}{4L} g(\mathrm{Tr}). \quad (21)$$

Eqn (21) demonstrates that the output power density P_{max}/A scales with the same functional dependence as the relative conductance $G_{el}/G_{el}{}^0$, consistent with the simulation results (Fig. 2e and 3e).

Both $P_{max}/P_{max}{}^0$ and P_{max}/A decrease monotonically with Tr according to g(Tr). However, the absolute value of P_{max} does not necessarily vary monotonically with Tr, depending on which structural dimension is held constant – analogous to the case of R_{el}. As shown in Fig. 7, P_{max} decreases with decreasing Tr when A_C decreases at fixed A, whereas it increases when A increases at fixed A_C. These trends arise directly from the corresponding dependencies of R_{el} (Fig. 4) and their previously discussed interpretation.

Under convective operating conditions, the combination of eqn (7) and (14) yields:

$$P_{max} = P_{max}{}^0 \left[\frac{hL/k}{G_{th}/G_{th}{}^0 + hL/k}\right]^2 (G_{el}/G_{el}{}^0) \quad (22)$$

or equivalently, using eqn (10) and (11):

$$P_{max} = P_{max}{}^0 \left[\frac{hL/k}{g(\mathrm{Tr}) + hL/k}\right]^2 g(\mathrm{Tr}). \quad (23)$$

Then, the output power density P_{max}/A can be expressed:

$$P_{max}/A = \frac{\sigma S^2 \Delta T_{max}{}^2}{4L} \left[\frac{hL/k}{G_{th}/G_{th}{}^0 + hL/k}\right]^2 (G_{el}/G_{el}{}^0) \quad (24)$$

or equivalently:

$$P_{max}/A = \frac{\sigma S^2 \Delta T_{max}{}^2}{4L} \left[\frac{hL/k}{g(\mathrm{Tr}) + hL/k}\right]^2 g(\mathrm{Tr}). \quad (25)$$

For uniform materials (Tr = 1), P_{max} decreases with decreasing convection coefficient h, due to the corresponding decrease in ΔT as expected by eqn (7) and (14) and illustrated by finite element calculations in Fig. 7. $P_{max}/P_{max}{}^0$ and P_{max}/A also decrease accordingly [eqn (22) and (24)]. Moreover, they are functions of g(Tr) and thus scale with *Transmissivity* [eqn (23) and (25)]. Corresponding finite element calculations are shown in Fig. 2e and 3e for P_{max}/A.

For constricted materials (Tr < 1), P_{max} may not vary monotonically with *Transmissivity* depending on which dimension is kept fixed, as explained in the case of R_{el}. Finite element calculations show that, contrary to the fixed ΔT case, under convective boundary conditions, $P_{max}/P_{max}{}^0$ and P_{max}/A may show non-monotonic variation with Tr. Such a non-monotonic dependence is illustrated in Fig. 3e for weak convection with h = 20 Wm^{-2} K^{-1}. In this case, P_{max}/A shows a maximum at an optimal *Transmissivity* $\mathrm{Tr}_{opt} \approx 0.09$. The non-monotonic dependence is depicted by the analytical formalism, eqn (23) and (25). These equations have global maximum when:

$$g(\mathrm{Tr}_{opt}) = \frac{hL}{k}. \quad (26)$$

At Tr_{opt}, $P_{max}/P_{max}{}^0$ and P_{max}/A reach their maxima. This result is confirmed by the finite element calculations. For example, applying this criterion to the dataset of Fig. 2b – where $g(\mathrm{Tr}) \approx \mathrm{Tr}^{0.5}$ – yields $\mathrm{Tr}_{opt} \approx 0.8$ for h = 200 Wm^{-2} K^{-1} and $\mathrm{Tr}_{opt} \approx 0.008$ for h = 20 Wm^{-2} K^{-1}, consistent with the simulation results (Fig. 2e). Similarly, applying it to the dataset of Fig. 3b – where $g(\mathrm{Tr}) \approx \mathrm{Tr}$ – yields $\mathrm{Tr}_{opt} \approx 0.9$ for h = 200 Wm^{-2} K^{-1} and $\mathrm{Tr}_{opt} \approx 0.09$ for h = 20 Wm^{-2} K^{-1}, again consistent with the simulation results (Fig. 3e).

Eqn (26) states that **$P_{max}/P_{max}{}^0$ and P_{max}/A are maximized when the functional g(Tr) equals the Biot number Bi (= hL/k).** The Biot number quantifies the balance between external con-

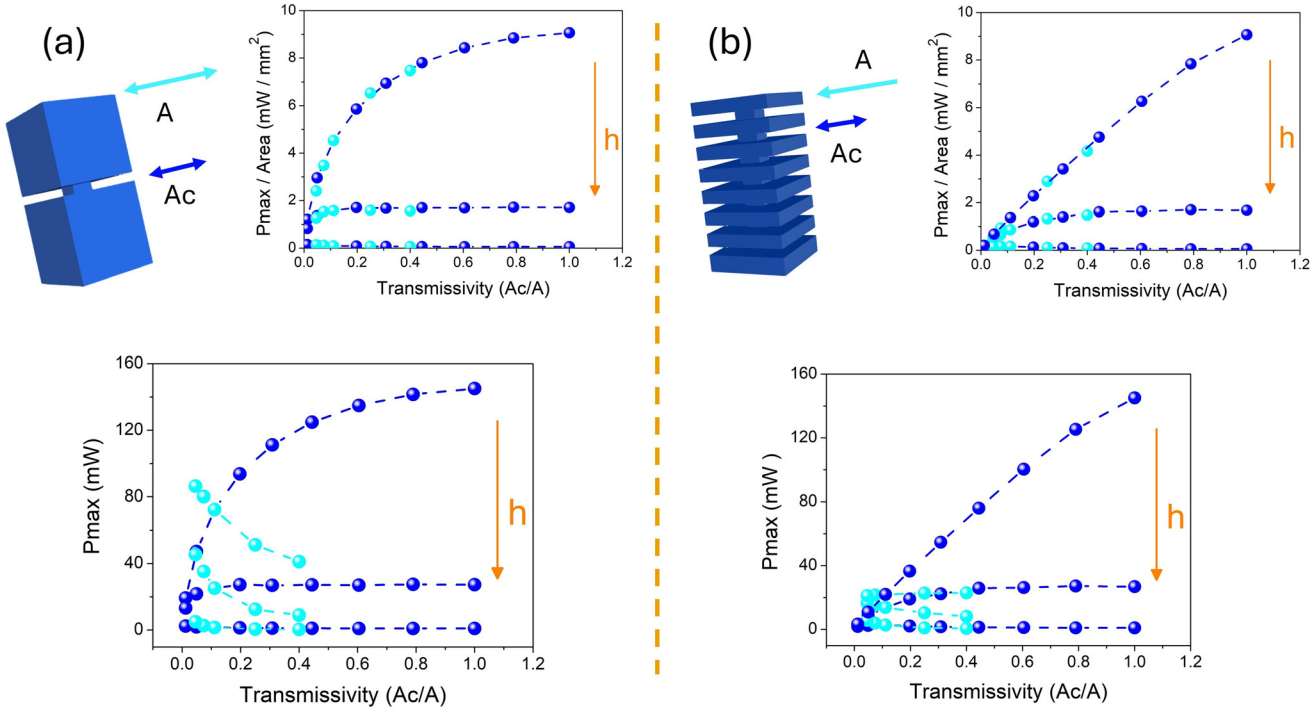

Fig. 7 Scaling of output power with Transmissivity. Absolute output power P_{max} and output power density P_{max}/A for (a) single-constriction modulation, and (b) multiple-constriction modulation, as in Fig. 4. Results are presented under three operating conditions for decreasing convection coefficient h: fixed ΔT ($h = \infty$), h = 200 Wm^{-2} K^{-1} and h = 20 Wm^{-2} K^{-1}.

vection and internal conduction. For strong convection, Bi ≈ 1 indicating that internal conduction is comparable to surface convection. In this regime, a significant temperature gradient is established across the material, and uniform-width geometry with high electrical conductance are optimal for maximizing TE output power. For weak convection, Bi << 1 indicating that internal heat conduction is much faster than external convection establishing nearly uniform temperature in the material. In this regime, a *constricted* geometry with low *Transmissivity* is preferred because it has decreased thermal conduction and thus preserves higher temperature gradient and enhanced output power.

The relevance of this condition for optimizing *constricted* geometries for maximum TE performance becomes even clearer when considering that: (i) *constricted* geometries consistently yield higher TE efficiency than uniform-width geometries due to enhanced ΔT under convective operating conditions, but (ii) the corresponding output power density does not necessarily increase, because while the reduced Tr boosts ΔT, it also increases the relative electrical resistance, partially offsetting the efficiency gains in efficiency. Therefore, maximizing TE performance ultimately requires maximizing output power density. In this context, eqn (26) provides the optimization criterion for designing constricted geometries for maximum output power and maximum TE performance under convective operating conditions. By applying eqn (26) to eqn (23) and (25) yields the optimal maximum output power P_{max}^{opt}, which can be expressed as follows:

$$P_{max}^{opt} = \frac{{P_{max}}^0}{4}\frac{hL}{k} \tag{27}$$

$$P_{max}^{opt}/A = \frac{\sigma S^2 {\Delta T_{max}}^2}{16L}\frac{hL}{k}. \tag{28}$$

Eqn (23), (25), and (26), along with their graphical representations (such as in Fig. 2e and 3e) constitute analytical TE Performance Desing Maps. These maps provide practical, predictive tools for evaluating *constricted* metamaterial geometries. They enable designers to determine, in advance, whether a certain *constricted* geometry will yield a net increase in output power, and if so, to quantify its magnitude for a given choice of geometric parameters and cross-sectional areas (A and A_C). Eqn (27) and (28) provide a means to calculate the maximum output power – and its density – attainable with the optimized *constricted* geometry. Eqn (27) can be rewritten in terms of the Biot number as:

$$P_{max}^{opt} = {P_{max}}^0\frac{\mathrm{Bi}}{4}. \tag{29}$$

Eqn (29) explicitly shows that the maximum output power of the optimal *constricted* geometry is inferior to that of the uniform geometry under fixed temperature difference by a factor of Bi/4.

The maximum power for the uniform, cuboid structure P_{max}^{cuboid} is obtained from eqn (23) by setting $g(Tr) = 1$:

$$P_{max}^{cuboid} = {P_{max}}^{0}\left[\frac{hL/k}{1+hL/k}\right]^{2}. \quad (30)$$

Eqn (29) and (30) give:

$$P_{max}^{opt} = P_{max}^{cuboid}\frac{(1+Bi)^{2}}{4Bi}. \quad (31)$$

Eqn (31) analytically shows that, under identical operating conditions, the optimal constricted geometry produces a maximum output power greater that that of the uniform (cuboid) geometry by a factor $(1 + Bi)^2/(4Bi)$. It consistently yields that $P_{max}^{opt} = P_{max}^{cuboid}$, for $Bi = g(Tr) = 1$ reflecting that the *cuboid* structure is preferable to the *constricted* geometry for efficient convective cooling.

3.4. Geometry optimization formalism, device-level factors and device design

The derived scaling formalism and the analytical optimization condition provide a rigorous and systematic scheme for optimizing the *constricted* geometry of a TE leg with cross-sectional area A and length L. The optimal constriction geometry – whether single or multiple-characterized by A_C^{opt}, can be obtained either graphically from the TE *Performance Design Maps* or numerically from the analytical condition $g(Tr) = Bi$ under the relevant operating conditions. This optimization scheme can be seamlessly integrated into standard TE device-optimization frameworks that account for additional device-level factors such as contact thermal resistance, electrode losses, and mechanical stability. In practice, the optimal TE leg dimensions A_{opt} and L_{opt} can be first determined using established device-level optimization methods, after which the optimal *constricted* geometry can be derived using our analytical criterion. This enables a truly global optimization of TE devices – something that has not been possible previously due to the absence of a validated optimization framework for *constricted* material geometries.

The importance of optimizing the material geometry as a prerequisite for optimizing composite TE legs – comprising both the *constricted* material and the contact resistances – was demonstrated in our recent work,[61] where the scaling formalism was used to interpret experimental observations on hourglass-shaped TE legs. In that study, we developed a unified optimization framework that incorporates both the *constricted* material and the contact electrodes. This analysis revealed that performance enhancements previously attributed to geometry modulation may, in fact, arise predominantly from contact resistance rather than from geometry alone. Moreover, the commonly used *geometric parameter*, which was employed to interpret the experiment, was shown to be an inappropriate metric for guiding the design of *constricted* legs: it violates current-continuity requirements and fails to capture the full influence of geometry modulation on electrical and thermal resistances. In contrast, this influence is fully governed by *Transmissivity* through its scaling relationship with transport properties, establishing it as a robust and physically sound descriptor of the impact of geometry modulation on TE performance.

To examine the effect of the contact thermal resistance R_{th}^{c} on the optimization condition – and on the resulting optimal *Transmissivity* – the Biot number of the composite leg, consisting of the leg and the two contact resistances, is expressed as:

$$Bi_{comp} = \frac{hL}{k_{comp}}. \quad (32)$$

The thermal resistance of the composite leg is:

$$R_{th}^{comp} = 2R_{th}^{c} + R_{th}. \quad (33)$$

Assuming that the contact thermal resistance per interface is a fraction f of the leg thermal resistance R_{th}, yields that:

$$R_{th}^{comp} = (1+2f)R_{th}. \quad (34)$$

It is thereby obtained that:

$$k_{comp} = k/(1+2f) \quad (35)$$

and

$$Bi_{comp} = (1+2f)Bi. \quad (36)$$

For well-designed TE modules, the contact thermal resistance per interface is a small fraction of the leg thermal resistance and neither the Biot number nor the optimal *Transmissivity* is expected to be significantly affected by contact thermal resistance. For instance, for contacts with thermal resistance equal to 5% of the leg thermal resistance, $f = 0.05$, $Bi_{comp} = 1.1Bi$, $Tr_{opt}^{comp} = 1.12Tr_{opt}$ for single constriction and $Tr_{opt}^{comp} = 1.1Tr_{opt}$ for multiple constrictions.

4. Conclusions

A universal scaling behavior of transport and key TE performance metrics with *Transmissivity* is demonstrated in width-modulated metamaterials with constrictions and expansions, spanning from the nanoscale to the macroscale, using analytical formalism and simulations across a range of modulation profiles with single and multiple constrictions.

Analytical formalism quantitatively interprets finite element calculations and shows explicitly that the effect of geometric modulation on temperature difference ΔT, electrical and thermal resistances, TE efficiency, and output power is governed by a single scaling function, $g(Tr)$ of the *Transmissivity* Tr. This function, defined by the ratio $G_{th(el)}/{G_{th(el)}}^{0}$, represents the (thermal/electrical) conductance of a *constricted* geometry relative to a uniform-width counterpart. Crucially, this relationship is independent of carrier type, material choice, exact constricted geometry profile and operating conditions. *Transmissivity* is thereby established as a reliable, multiscale design parameter for engineering transport properties – analogous to nature's use of hierarchical structures to achieve optimized functionality.

Constricted geometries consistently enhance TE efficiency compared to uniform-width structures – primarily through

increased ΔT under convective operating conditions. However, this enhancement does not always translate into higher output power. The analytical scaling formalism for the output power density together with its graphical representation, constitute *TE Performance Design Maps* – practical, predictive tools that identify the conditions under which constricted geometries can enhance TE performance. Furthermore, an analytical optimization criterion is established: maximum TE performance is achieved at an optimal *Transmissivity*, Tr_{opt}, where $g(\mathrm{Tr}_{opt}) = \mathrm{Bi}$, with $\mathrm{Bi} = hL/k$ the Biot number. The optimization condition leads to the generic conclusion that compared with the uniform geometry, the optimal constricted geometry produces a maximum output power reduced under fixed ΔT, by a factor of Bi/4, and enhanced under identical convective operating conditions by a factor of $(1 + \mathrm{Bi})^2/(4\mathrm{Bi})$.

Although the physical meaning of the Biot number is well established in thermal science, its connection to a geometry-dependent scaling function and its use as an analytical optimization condition for constricted TE legs have not been previously reported. The condition $g(\mathrm{Tr}_{opt}) = \mathrm{Bi}$ emerges uniquely from the common scaling of electrical and thermal conductance with *Transmissivity* – an insight introduced here for the first time. Unlike previous models based on equivalent resistances, which can inadvertently neglect current continuity requirements, our formalism provides a mathematically rigorous design rule. The criterion $g(\mathrm{Tr}_{opt}) = \mathrm{Bi}$ therefore provides the first explicit, closed-form optimization condition for geometry-modulated TE legs.

The universal scaling formalism provides a rigorous framework for evaluating TE performance in *constricted* metamaterials and establishes the foundation for a unified optimization strategy for composite TE legs that incorporate both metamaterial and electrode contacts. Beyond establishing this universal framework, our results provide the missing analytical tools required to integrate geometry-modulated legs into full device-level optimization workflows. By enabling the systematic determination of optimal *constricted* geometries and their coupling with contact and module-level constraints, the present formalism offers a practical pathway toward globally optimized thermoelectric devices – an advance that was previously not achievable due to the absence of a validated optimization strategy for geometry-modulated materials.

This work offers a theoretical platform for multiscale design and optimization of *constricted* geometries, enabling systematic exploration of design strategies for next-generation TE modules based on advanced thermoelectric metamaterials.

Author contributions

X. Z.: conceptualization; methodology, investigation, formal analysis, visualization, writing.

Conflicts of interest

There are no conflicts to declare.

Data availability

The data that support the findings of this study are included in the article.

Appendix A: Analytical formalism for the temperature difference ΔT in uniform and non-uniform materials under convective operation conditions

Let us consider a uniform cuboid material of cross-sectional area A and length L. For a hot-side temperature T_h, the cold-side temperature T_c under convective conditions is determined by the solution of the 1D steady-state thermal conduction equation:

$$\frac{d^2T}{dx^2} = 0 \Rightarrow T(x) = C_1x + C_2 \tag{37}$$

where constants C_1 and C_2 are determined applying the boundary conditions:

$$T(0) = T_h \tag{38}$$

$$-k\frac{dT}{dx}|_{x=L} = h[T(L) - T_a] \tag{39}$$

where k is the material thermal conductivity, h is the convection coefficient and T_a is the ambient temperature. This gives:

$$T_c = T_h - \frac{hL}{k + hL}(T_h - T_a). \tag{40}$$

For corresponding non-uniform materials, eqn (40) can be extended as follows:

$$T_c = T_h - \frac{hL}{k_{eff} + hL}(T_h - T_a) \tag{41}$$

in terms of the effective thermal conductivity k_{eff}, defined from the non-uniform material's thermal conductance G_{th} through the relation:

$$G_{th} = k_{eff}\frac{A}{L}. \tag{42}$$

The intrinsic thermal conductivity k and the thermal conductance of the uniform cuboid material ${G_{th}}^0$ are related by the expression:

$${G_{th}}^0 = k\frac{A}{L}. \tag{43}$$

Combining eqn (42) and (43) yields:

$$\frac{k_{eff}}{k} = \frac{G_{th}}{{G_{th}}^0} = \frac{{R_{th}}^0}{R_{th}}. \tag{44}$$

Then, from eqn (41) and (44), it is obtained:

$$\Delta T = \frac{hL/k}{k_{eff}/k + hL/k}(T_h - T_a) \tag{45}$$

or equivalently expressed, in terms of $\Delta T_{max} \equiv T_h - T_a$:

$$\Delta T = \frac{hL/k}{G_{th}/G_{th}{}^0 + hL/k}\Delta T_{max} = \frac{hL/k}{R_{th}{}^0/R_{th} + hL/k}\Delta T_{max}. \quad (46)$$

References

1 F. J. DiSalvio, Thermoelectric Cooling and Power Generation, *Science*, 1999, **285**, 703–706.
2 *Thermoelectrics Handbook: Macro to Nano*, ed. D. M. Rowe, CRC Press, Boca Raton, FL, 2006.
3 J. He and T. M. Tritt, Advances in Thermoelectric Materials Research: Looking Back and Moving Forward, *Science*, 2017, **357**, eaak9997.
4 A. Zevalkink, D. M. Smiadak, J. L. Blackburn, A. J. Ferguson, M. L. Chabinyc, O. Delaire, J. Wang, K. Kovnir, J. Martin, L. T. Schelhas, T. D. Sparks, S. D. Kang, M. T. Dylla, G. J. Snyder, B. R. Ortiz and E. S. Toberer, A Practical Field Guide to Thermoelectrics: Fundamentals, Synthesis, and Characterization, *Appl. Phys. Rev.*, 2018, **5**, 021303.
5 D. Beretta, N. Neophytou, J. M. Hodges, M. G. Kanatzidis, D. Narducci, M. Martin-Gonzalez, M. Beekman, B. Balke, G. Cerretti, W. Tremel, A. Zevalkink, A. I. Hofmann, C. Müller, B. Dörling, M. Campoy-Quiles and M. Caironi, Thermoelectrics: From History, a Window to the Future, *Mater. Sci. Eng., R*, 2019, **138**, 100501.
6 D. Narducci and F. Giulio, Recent Advances on Thermoelectric Silicon for Low-Temperature Applications, *Materials*, 2022, **15**, 1214.
7 A. Kim, J. Lee, J. Park, W. Kim, S. Lee, J. Kim, J. Y. Lee and Y. Kim, Recent Advances in the Nanomaterials, Design, Fabrication Approaches of Thermoelectric Nanogenerators for Various Applications, *Adv. Mater. Interfaces*, 2022, **9**, 2201659.
8 T. Hendricks, T. Caillat and T. Mori, Keynote Review of Latest Advances in Thermoelectric Generation Materials, Devices, and Technologies 2022, *Energies*, 2022, **15**, 7307.
9 A. Dadhich, M. Saminathan, K. Kumari, S. Perumal, M. S. Ramachandra Rao and K. Sethupathi, Physics and Technology of Thermoelectric Materials and Devices, *J. Phys. D: Appl. Phys.*, 2023, **56**, 333001.
10 S. Yang, H. Chen and D. Luo, A Comprehensive Review of Thermoelectric Generators from Micropower Supply to Kilowatt System, *Green Energy Fuel Res.*, 2025, **2**, 93–108.
11 H. J. Goldsmid, Principles of Thermoelectric Devices, *Br. J. Appl. Phys.*, 1960, **11**, 209–217.
12 G. Min and D. M. Rowe, Optimisation of Thermoelectric Module Geometry for 'Waste Heat' Electric Power Generation, *J. Power Sources*, 1992, **38**, 253–259.
13 G. Zhang, L. Fan, Z. Niu, K. Jiao, H. Diao, Q. Du and G. Shu, A Comprehensive Design Method for Segmented Thermoelectric Generator, *Energy Convers. Manage.*, 2015, **106**, 510–519.
14 H. J. Goldsmid, *The Physics of Thermoelectric Energy Conversion*, IOP Publishing, Bristol, UK, 2017.
15 L. E. Bell, Cooling, Heating, Generating Power, and Recovering Waste Heat with Thermoelectric Systems, *Science*, 2008, **321**, 1457–1461.
16 D. Luo, H. Chen, W.-H. Chen, X. Zhang, L. Geng, W. Jiang, Y. Yu and B. Y. Cao, Interdependent Optimization Strategies for Material, Module, and System Designs in Thermoelectric Devices, *Device*, 2025, **3**, 100752.
17 S. Asaadi, S. Khalilarya and S. Jafarmadar, A Thermodynamic and Exergoeconomic Numerical Study of Two-Stage Annular Thermoelectric Generator, *Appl. Therm. Eng.*, 2019, **156**, 371–381.
18 M.-W. Tian, L. W. W. Mihardjo, H. Moria, S. Asaadi, H. Sadighi Dizaji, S. Khalilarya and P. T. Nguyen, A Comprehensive Energy Efficiency Study of Segmented Annular Thermoelectric Generator: Thermal, Exergetic, and Economic Analysis, *Appl. Therm. Eng.*, 2020, **181**, 115996.
19 M.-W. Tian, L. W. W. Mihardjo, H. Moria, S. Asaadi, S. Pourhedayat, H. Sadighi Dizaji and M. Wae-hayee, Economy, Energy, Exergy, and Mechanical Study of Co-Axial Ring Shape Configuration of Legs as a Novel Structure for Cylindrical Thermoelectric Generator, *Appl. Therm. Eng.*, 2021, **184**, 116274.
20 L. Fan, G. Zhang, R. Wang and K. Jiao, A Comprehensive and Time-Efficient Model for Determination of Thermoelectric Generator Length and Cross-Section Area, *Energy Convers. Manage.*, 2016, **122**, 85–94.
21 J. A. Brandt, *Advanced Energy Conversion*, Pergamon Press, Oxford, 1962, vol. 2, pp. 219–230.
22 V. A. Semenyuk, Efficiency of Cooling Thermoelectric Elements of Arbitrary Shape, *J. Eng. Phys. Thermophys.*, 1977, **32**, 196–200.
23 G. Fraisse, M. Lazard, C. Goupil and J. Y. Serrat, Study of a Thermoelement's Behaviour through a Modelling Based on Electrical Analogy, *Int. J. Heat Mass Transfer*, 2010, **53**, 3503–3512.
24 X. Zianni, Diameter-Modulated Nanowires as Candidates for High Thermoelectric Energy Conversion Efficiency, *Appl. Phys. Lett.*, 2010, **97**, 233106.
25 X. Zianni, Efficient Thermoelectric Energy Conversion on Quasi-Localized Electron States in Diameter Modulated Nanowires, *Nanoscale Res. Lett.*, 2011, **6**, 286.
26 X. Zianni, The Effect of the Modulation Shape in the Ballistic Thermal Conductance of Modulated Nanowires, *J. Solid State Chem.*, 2012, **193**, 53–57.
27 X. Zianni and P. Chantrenne, Thermal Conductivity of Diameter-Modulated Silicon Nanowires Within a Frequency-Dependent Model for Phonon Boundary Scattering, *J. Electron. Mater.*, 2012, **42**, 1509–1513.
28 X. Zianni, V. Jean, K. Termentzidis and D. Lacroix, Scaling Behavior of the Thermal Conductivity of Width-Modulated Nanowires and Nanofilms for Heat Transfer Control at the Nanoscale, *Nanotechnology*, 2014, **25**, 465402.
29 A. S. Al-Merbati, B. S. Yilbas and A. Z. Sahin, Thermodynamics and Thermal Stress Analysis of

Thermoelectric Power Generator: Influence of Pin Geometry on Device Performance, *Appl. Therm. Eng.*, 2013, **50**, 683–692.
30 A. Z. Sahin and B. S. Yilbas, The Thermoelement as Thermoelectric Power Generator: Effect of Leg Geometry on the Efficiency and Power Generation, *Energy Convers. Manage.*, 2013, **65**, 26–32.
31 U. Erturun, K. Erermis and K. Mossi, Effect of Various Leg Geometries on Thermo-Mechanical and Power Generation Performance of Thermoelectric Devices, *Appl. Therm. Eng.*, 2014, **73**, 128–141.
32 R. Lamba and S. C. Kaushik, Thermodynamic Analysis of Thermoelectric Generator Including Influence of Thomson Effect and Leg Geometry Configuration, *Energy Convers. Manage.*, 2017, **144**, 388–398.
33 H. Ali, A. Z. Sahin and B. S. Yilbas, Thermodynamic Analysis of a Thermoelectric Power Generator in Relation to Geometric Configuration Device Pins, *Energy Convers. Manage.*, 2014, **78**, 634–640.
34 B. S. Yilbas and H. Ali, Thermoelectric Generator Performance Analysis: Influence of Pin Tapering on the First and Second Law Efficiencies, *Energy Convers. Manage.*, 2015, **100**, 138–146.
35 O. I. Ibeagwu, Modelling and Comprehensive Analysis of TEGs with Diverse Variable Leg Geometry, *Energy*, 2019, **180**, 90–106.
36 A. Fabián-Mijangos, G. Min and J. Alvarez-Quintana, Enhanced Performance Thermoelectric Module Having Asymmetrical Legs, *Energy Convers. Manage.*, 2017, **148**, 1372–1381.
37 S. Choo, J. Lee, B. Şişik, S.-J. Jung, K. Kim, S. E. Yang, S. Jo, C. Nam, S. Ahn, H. S. Lee, H. G. Chae, S. K. Kim, S. LeBlanc and J. S. Son, Geometric Design of Cu_2 Se-Based Thermoelectric Materials for Enhancing Power Generation, *Nat. Energy*, 2024, **9**, 1105–1116.
38 H.-B. Liu, J.-H. Meng, X.-D. Wang and W.-H. Chen, A New Design of Solar Thermoelectric Generator with Combination of Segmented Materials and Asymmetrical Legs, *Energy Convers. Manage.*, 2018, **175**, 11–20.
39 S. Shittu, G. Li, X. Zhao, X. Ma, Y. Golizadeh Akhlaghi and E. Ayodele, Optimized High Performance Thermoelectric Generator with Combined Segmented and Asymmetrical Legs under Pulsed Heat Input Power, *J. Power Sources*, 2019, **428**, 53–66.
40 Y. Thimont and S. LeBlanc, The Impact of Thermoelectric Leg Geometries on Thermal Resistance and Power Output, *J. Appl. Phys.*, 2019, **126**, 095101.
41 B. Şişik and S. LeBlanc, The Influence of Leg Shape on Thermoelectric Performance Under Constant Temperature and Heat Flux Boundary Conditions, *Front. Mater.*, 2020, **7**, 595955.
42 S. Shittu, G. Li, X. Zhao and X. Ma, Review of Thermoelectric Geometry and Structure Optimization for Performance Enhancement, *Appl. Energy*, 2020, **268**, 115075.
43 H.-B. Liu, S.-L. Wang, Y.-R. Yang, W.-H. Chen and X.-D. Wang, Theoretical Analysis of Performance of Variable Cross-Section Thermoelectric Generators: Effects of Shape Factor and Thermal Boundary Conditions, *Energy*, 2020, **201**, 117660.
44 S. Sathiyamoorthy, R. Kumar, B. Neppolian, S. Dhanalakshmi and P. Veluswamy, Design and Optimization of Thermoelectric Devices Toward Geometric Aspects and a Promising Electrode for Room-Temperature Wearable Applications, *ECS J. Solid State Sci. Technol.*, 2021, **10**, 071022.
45 Q. Meng, Q. Ni and X. Song, The Evaluation of Power Generation Performance of Variable Cross Section Thermoelectric Generator Based on New Thermoelectric Material Parameter Measurement Method, *Energy Sources, Part A*, 2021, **47**, 11734–11748.
46 A. Khalil, A. Elhassnaoui, S. Yadir, O. Abdellatif, Y. Errami and S. Sahnoun, Performance Comparison of TEGs for Diverse Variable Leg Geometry with the Same Leg Volume, *Energy*, 2021, **224**, 119967.
47 Y. Tao, Z.-M. Li, P. Peng, W. Liu, Y.-Y. Shao and Z.-Z. He, Performance Analysis and Design Optimization of a Compact Thermoelectric Generator with T-Shaped Configuration, *Energy*, 2021, **229**, 120652.
48 C. Maduabuchi, Improving the Performance of a Solar Thermoelectric Generator Using Nano-Enhanced Variable Area Pins, *Appl. Therm. Eng.*, 2022, **206**, 118086.
49 J. Liu, Y. Sun, G. Chen and P. Zhai, Performance Analysis of Variable Cross-Section TEGs under Constant Heat Flux Conditions, *Energies*, 2023, **16**, 4473.
50 Y. Lan, J. Lu and S. Wang, Study of the Geometry and Structure of a Thermoelectric Leg with Variable Material Properties and Side Heat Dissipation Based on Thermodynamic, Economic, and Environmental Analysis, *Energy*, 2023, **282**, 128895.
51 J. Chen, R. Wang, R. Ding, W. Liu, Y. Jiang and D. Luo, Innovative Design and Numerical Optimization of a Cylindrical Thermoelectric Generator for Vehicle Waste Heat Recovery, *Energy Convers. Manage.*, 2025, **326**, 119478.
52 S. Yang, H. Chen and D. Luo, Advanced Bifurcated Fin Design with Diversion Channels for Optimizing Output Performance of Thermoelectric Generators, *Int. Commun. Heat Mass Transfer*, 2025, **165**, 109078.
53 Y.-Q. Zhang, J. Sun, G.-X. Wang and T.-H. Wang, Advantage of a Thermoelectric Generator with Hybridization of Segmented Materials and Irregularly Variable Cross-Section Design, *Energies*, 2022, **15**, 2944.
54 K. Bun, S. S. Rapaka, S. Pathak, A. Date and S. Wang, Additive Manufacturing, Topology Optimization of Thermoelectric Generators, and Beyond: A Comprehensive Review on Pioneering Thermoelectric Conversion for a Sustainable Future, *Appl. Therm. Eng.*, 2025, **278**, 127437.
55 S. Yang, H. Chen and D. Luo, A Comprehensive Review of Thermoelectric Generators from Micropower Supply to Kilowatt System, *Green Energy Fuel Res.*, 2025, **2**, 93–108.
56 D. R. Karana and R. R. Sahoo, Influence of Geometric Parameter on the Performance of a New Asymmetrical and

Segmented Thermoelectric Generator, *Energy*, 2019, **179**, 90–99.

57 P. Wang, B. Wang, K. Wang, R. Gao and L. Xi, An Analytical Model for Performance Prediction and Optimization of Thermoelectric Generators with Varied Leg Cross-Sections, *Int. J. Heat Mass Transfer*, 2021, **174**, 121292.

58 H. He, Y. Xie, Q. Zuo, W. Chen, Z. Shen, Y. Ma, H. Zhang, G. Zhu and Y. Ouyang, Optimization Analysis for Thermoelectric Performance Improvement of Biconical Segmented Annular Thermoelectric Generator, *Energy*, 2024, **306**, 132397.

59 X. Zianni, Thermoelectric Metamaterials: Nano-Waveguides for Thermoelectric Energy Conversion and Heat Management at the Nanoscale, *Adv. Electron. Mater.*, 2021, **7**, 2100176.

60 X. Chen, F. Cai, R. Dong, X. Lei, R. Sui, L. Qiu, Z. Zeng, W. Sun, H. Zheng and Q. Zhang, Enhanced Thermoelectric Properties of n-Type $Bi_2Te_{2.7}Se_{,0.3}$ for Power Generation, *J. Mater. Sci.: Mater. Electron.*, 2020, **31**, 4924–4930.

61 X. Zianni, Optimal geometric design of thermoelectric metamaterials for enhancing power generation: An interpretative approach, *J. Appl. Phys.*, 2025, **138**, 165101.

62 B. H. Silva, D. Lacroix, M. Isaiev and L. Chaput, Monte Carlo simulation of phonon transport from ab-initio data with Nano-, *Comput. Phys. Commun.*, 2024, **294**, 108954. Developer's repository link: https://github.com/brunohs1993/Nanokappa.

63 X. Zianni, Geometry Modulated Metamaterials for Enhanced Thermoelectric Effects and Decreased Thermal Conduction, *MRS Adv.*, 2021, **6**, 707–712.

64 X. Zianni, K. Termentzidis and D. Lacroix, On the dependence of the thermal conductivity of width-modulated nanowires on the number of modulations, *J. Phys.:Conf. Ser.*, 2017, **785**, 012011.